

# Creep Behavior of Double Tempered 8%Cr-2%WVTa Martensitic Steel

Manabu Tamura<sup>1</sup>, Matthew M. Nowell<sup>2</sup>, Kei Shinozuka<sup>1</sup> and Hisao Esaka<sup>1</sup>

<sup>1</sup>Department of Materials Science and Engineering, National Defense Academy, Yokosuka 239-8686, Japan

<sup>2</sup>TSL Inc., 392 East 12300 South, Suite H Draper, Utah, 84020, USA

Creep testing was carried out at around 650°C for a martensitic 8Cr-2WVTa steel (F82H), which is a candidate alloy for the first wall of the fusion reactors of the Tokamak type. Rupture strength of the double tempered steel (F82HD) is lightly higher than that of simply tempered steel (F82HS). On the other hand, creep rate of F82HD is obviously smaller than that of F82HS in acceleration creep, though creep strain of F82HD in transition creep, where creep rate decreases with increasing strain, is larger than that of F82HS. Hardness of the crept F82HD decreases with increasing creep strain, which corresponded with the transmission electron microscopy (TEM) observation. On the contrary, X-ray diffraction and electron back-scattered diffraction pattern measurements show that fine sub-grains are created during transition creep. The creep curves were analyzed using an exponential type creep equation and the apparent activation energy, the activation volume and the pre-exponential factor were calculated as a function of creep strain. Then, these parameters were converted into two parameters, *i.e.* equivalent obstacle spacing (EOS) and mobile dislocation density parameter (MDDP). While EOS decreases with increasing creep strain, MDDP increases with increasing strain during transition creep. The decrease in EOS and the increase in either EOS or MDDP are rate-controlling factors in transition and acceleration creep, respectively. On the other hand, in case of F82HS, EOS increases and MDDP decreases during transition creep. In this case, the decrease in MDDP controls the creep rate during transition creep of F82HS. It is concluded that both EOS and MDDP are representative parameters of the change in substructure during creep. [doi:10.2320/matertrans.47.1332]

(Received December 13, 2005; Accepted March 22, 2006; Published May 15, 2006)

**Keywords:** ferritic heat resistant steel, creep, electron back-scattered diffraction pattern, X-ray diffraction, activation energy, fusion reactor, tempering

## 1. Introduction

The construction site of International Thermonuclear Experimental Reactor (ITER) was narrowed down to Cadarache, France in July 2005. Steel of F82H<sup>1-3)</sup> is planned to use for a Japanese ITER test blanket module.<sup>4)</sup> According to the trial design the test blanket is fabricated by mainly hot isostatic pressing and tungsten inert gas welding<sup>5)</sup> and the total mass of a unit module exceeds 2 ton.<sup>6)</sup> Therefore, heating rate of tempering after hiping is considered to be very small. It is well known that high alloy steel shows secondary hardening near 500°C<sup>7)</sup> and, therefore, heating rate may affect the creep strength as well. For these cases double tempering has been adopted in order to stabilize the microstructures,<sup>8,9)</sup> however, the metallurgical explanation for the double tempering is insufficient.

A very large database including rupture data for F82H has been constructed under the international collaborative work.<sup>10-12)</sup> However, creep behavior of the steel has not been clarified sufficiently, while structural steel should not be used in a strain range of acceleration creep. Therefore, the effect of secondary hardening on creep behavior of F82H should be studied further from the engineering viewpoint.

Creep behavior of F82H tempered by two steps (F82HD) has been studied comparing with the behavior of the simply tempered one (F82HS). The substructures of creep-interrupted specimens have been studied in detail only for F82HD, because the metallurgical changes in the usually normalized and tempered martensitic steel, like F82HS, are reported in the literatures.<sup>13-17)</sup>

## 2. Experimental Procedure

A 15 mm mill production plate of F82H<sup>18)</sup> was used. Chemical composition of the plate is shown in Table 1. The

heat treatment applied and Vickers hardness numbers are also shown in the table. The plate of F82H was re-normalized at 1200°C for 30 min followed by pre-tempered at 550°C for 15 h and final tempering at 800°C for 2 h. Normalized and tempered plate of F82H without pre-tempering were also used. Extracted residues using a 0.1 µm membrane filter for both F82HD and F82HS were analyzed by X-ray diffraction (XRD).

Test pieces with 6 mm diameter and 30 mm gauge length were machined from the test plates and creep testing was carried out at around 650°C in air under a constant load. Creep interruption tests were made at 650°C under 78 MPa for F82HD. A TEM disc was taken from a crept specimen of F82HD and the thin film was observed using HF2000. Cross sections of the crept specimens were polished using a 800 grit SiC paper and finally surface layer of 0.3 mm was removed electrically. And, integrated widths of (110), (200), (211), (220) and (310) X-ray diffraction peaks of the matrix were measured. The X-ray integrated widths for the matrix peaks were analyzed using the Hall's relation<sup>19)</sup> and both particle size,  $\delta$ , and lattice strain,  $\eta$ , were calculated. In the analysis the standard Si powder made by National Institute of Standards and Technology was used as a reference material. In order to visualize the changes in the particle size measured by XRD, electron backscattered diffraction pattern (EBSP) measurements were performed for F82HD using a scanning electron microscope of a field emission type (FE-SEM; FEI XL-30 FEG). For the EBSP measurements samples were repolished using 0.05 µm colloidal silica for about 60 min after polishing using 0.3 µm Al<sub>2</sub>O<sub>3</sub> abrasives. Sample normal crystal direction maps at 85X, 850X and 8500X magnification (2000, 100 and 20 nm for each step and 500, 2000 and 500,000 data-points/sample, respectively), grain maps with misorientation levels of 0.5, 1 and 5 degrees and grain size histograms were obtained.

Table 1 Chemical composition and heat treatment of the experimental steels.

| Steel | Chemical composition (mass%) |     |      |      |     |      |     |       | Heat treatment ( $^{\circ}\text{C} \times \text{h}$ ) |                 |                | HV10 |
|-------|------------------------------|-----|------|------|-----|------|-----|-------|---|-----------------|----------------|------|
|       | C                            | Si  | Mn   | Cr   | V   | Ta   | W   | N     | Normalizing   | Pre-tempering   | Tempering      |      |
| F82HD | 0.096                        | 0.1 | 0.15 | 7.71 | 0.2 | 0.04 | 2.1 | 0.004 | $1200 \times 0.5$                                     | $550 \times 15$ | $800 \times 2$ | 175  |
| F82HS |                              |     |      |      |     |      |     |       |   | —               |                | 172  |

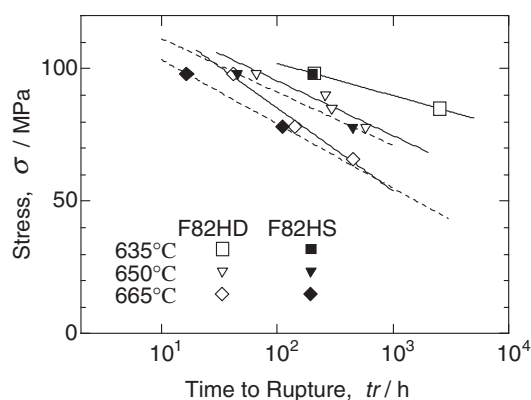


Fig. 1 Time to rupture vs. stress diagram for F82HD and F82HS.

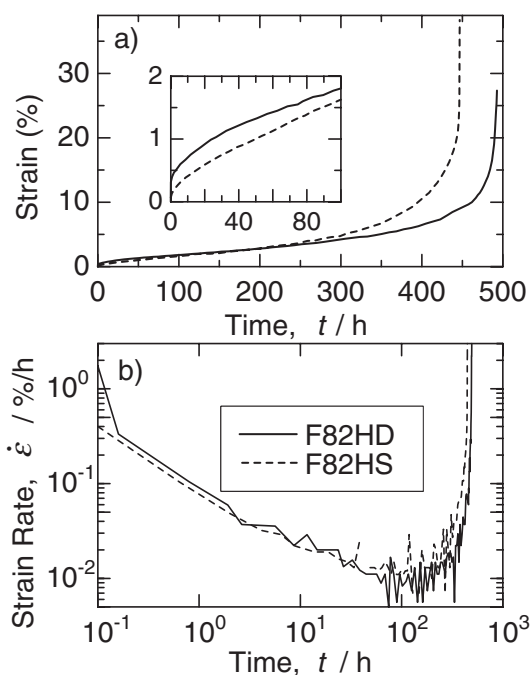
### 3. Experimental Results

#### 3.1 Microstructure

Tempered martensite covered uniformly the polished surfaces of both F82HD and F82HS. X-ray analysis for the extracted residues of both steels showed that major precipitate was  $\text{M}_{23}\text{C}_6$  and most of Ta was found as  $\text{TaO}_2$  with very small amount of TaC. Particle size calculated from the X-ray integrated widths of three major peaks of  $\text{TaO}_2$  was about 39 nm. This value is comparable with the size of Ta-rich particles observed on the replicas of the thermally aged specimens for 30000 h at  $600^{\circ}\text{C}$  and  $650^{\circ}\text{C}$ , 17–27 nm.<sup>20)</sup> Particle size calculated from the integrated width for  $\text{M}_{23}\text{C}_6$  for F82HS was 76 nm. A peak with a bump was observed for F82HD. A (511) peak of  $\text{M}_{23}\text{C}_6$  for F82HD was decomposed into two peaks assuming normal distribution of intensity and the calculated particle sizes were 67 and 35 nm for high and low diffraction angles, respectively. The thermo-dynamical calculation system<sup>21)</sup> and Powder Diffraction File of the International Center for Diffraction Data suggest that  $\text{M}_{23}\text{C}_6$  formed at  $800^{\circ}\text{C}$  contains larger amount of iron than that of  $550^{\circ}\text{C}$ . It can be concluded that F82HD contains two kinds of  $\text{M}_{23}\text{C}_6$ , *i.e.* larger size with higher content of iron and smaller size one with lesser iron content and the smaller one was formed during pre-tempering at  $550^{\circ}\text{C}$ .

#### 3.2 Rupture strength and creep curves

Figure 1 shows the relation between stress and time to rupture for F82HD and F82HS. Rupture strength of F82HD approaches to that of F82HS at  $665^{\circ}\text{C}$  and 300 h. On the other hand, rupture strength of F82HD at  $650^{\circ}\text{C}$  is higher than that of F82HS. Creep curves and creep rate vs. time curves for both steels obtained at  $650^{\circ}\text{C}$  and 78 MPa are shown in Fig. 2. Instantaneous strain of F82HD shown in Fig. 2 is rather large as compared with that of F82HS. Instantaneous

Fig. 2 (a) Creep curves and (b) creep rate vs. time curves for F82HD and F82HS tested at  $650^{\circ}\text{C}$  and 78 MPa.

strain includes elastic strain and instantaneous plastic strain. Inadequate adjustment of a strain detector can cause unexpected displacement. However, instantaneous strains for the creep-interrupted specimens of F82HD tested under the same condition were rather large as compared with that of F82HS. Therefore, the rather large instantaneous strain of F82HD may be caused by the test condition that the stress may be near the yield stress of F82HD. However, as mentioned later we cannot find any evidences for work hardening due to the rather large instantaneous strain by hardness test and TEM observation for the 0.36% crept F82HD. Therefore, the rather large instantaneous strain of F82HD is considered to affect little on the creep behavior. Creep rate of F82HD in transition range is lightly larger than that of F82HS and minimum creep rate was found when the strain was about 2% for both steels. However, Fig. 2 shows that creep rate of F82HD in acceleration range becomes lower than F82HS. Therefore, it can be said that creep behavior of F82HD obviously differs from that of F82HS, though the rupture strength of F82HD is only lightly larger than that of F82HS. The origin for this is not only the difference in dislocation structure of tempered martensite but also the finer distribution of  $\text{M}_{23}\text{C}_6$  as mentioned in the previous section. Therefore, long-term creep behavior under irradiation should be clarified using F82H the heat treatment of which is simulating the fabrication conditions of the test blanket module for ITER.

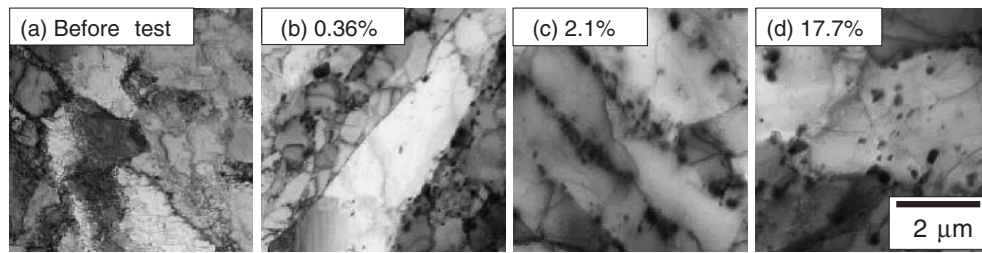


Fig. 3 Transmission electron microstructures of F82HD crept at 650°C and 78 MPa. Number in each photograph indicates creep strain.

### 3.3 Creep interruption test for F82HD

#### 3.3.1 Hardness

Hardness for F82HD at room temperature decreases with increasing strain through the whole range of the creep curve. Data are shown later (Fig. 12).

#### 3.3.2 TEM

Figure 3 shows TEM microstructures for F82HD revealing that tangled dislocations within lath boundaries are swept out in an early stage of creep deformation, lath boundaries are pinned by large precipitates at minimum creep rate, *i.e.* 2% of creep strain, lath martensite begins to coalesce with each other in acceleration creep and finally sub-grains of about  $3.5\mu\text{m}^{22)}$  are formed. These observations qualitatively coincide with the changes in TEM microstructures of the high Cr tempered martensitic steels.<sup>13–17)</sup>

#### 3.3.3 Particle size measured by X-ray

X-ray diffraction peaks are broadened by many kinds of defects. Both elastic strain distributed locally in a specimen including elastic strain due to dislocations and grain size are the major causes of the line broadening. The elastic strain and the grain size can be calculated from the integrated breadths for matrix diffraction peaks using a Hall's plot.<sup>19)</sup> The grain size denotes the size of the unstrained perfect crystal in a specimen assuming that Si powder is perfect crystal with infinite size. Obviously, the grain size should have a different physical meaning from grain size observed under an optical and electron microscope. Therefore, the grain size obtained by X-ray is called particle size.

Both particle size,  $\delta$ , and elastic strain,  $\eta$ , for the electrically polished F82HD are shown in Fig. 4 as a function of creep strain. Total strain is plotted as creep strain in the horizontal axis, because it is difficult to separate creep strain from total strain. Then, total strain is treated as creep strain, hereinafter. When the inverse value of y-axis in a Hall's plot is smaller than  $1/5\mu\text{m}$  or negative, particle size is plotted at  $5\mu\text{m}$ , because the particle size of the reference material, Si powder, is  $5\mu\text{m}$ . When  $\delta$  is large,  $\eta$  is also large, and *vice versa*, in general. This trend is re-confirmed in the figure and, therefore, the change in the corrected particle size shown in the figure may be reasonable. Both  $\delta$  and  $\eta$  increase and then decrease with increasing creep strain, *i.e.* the maximum  $\delta$  and  $\eta$  are found at 0.36% and both  $\delta$  and  $\eta$  show minimum at minimum creep rate. In acceleration creep range, similar peaks in both  $\delta$  and  $\eta$  are observed at 10% of creep strain.

Integrated widths of the specimens for EBSD, mentioned in the next section, were also measured. Both  $\delta$  and  $\eta$  obtained for the EBSD specimens are smaller and larger than these for electrically polished ones, respectively. This means that the surface is damaged to some extent, even after polishing for

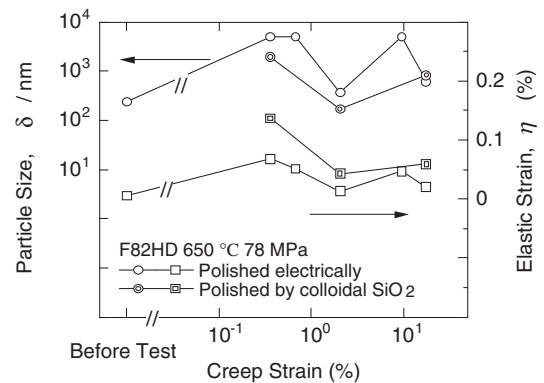


Fig. 4 Particle size,  $\delta$ , and local elastic strain,  $\eta$ , as a function of creep strain, which are calculated from integrated widths using the Hall's relation.

1 h using colloidal  $\text{SiO}_2$ . However, under the existing technical circumstances, flatness of the observed surface is essential for EBSD measurement and, therefore, electrical polishing is unsuitable for EBSD measurement. Nevertheless, the trend of the changes in both  $\delta$  and  $\eta$  for both electrical and  $\text{SiO}_2$  polishing is quite similar and the differences between them are relatively small. Therefore, mechanical polishing by  $\text{SiO}_2$  might affect little on the EBSD measurements.

#### 3.3.4 Sub-grain size by EBSD measurement

The sample normal crystal direction maps for the crept F82HD at 650°C and 78 MPa up to the strains of 0.36, 2.1 and 17.7%, respectively, are shown in Fig. 5. The inverse pole figure measurements showed that the tensile axis for the 0.36, 2.1 and 17.7% crept specimens nearly faced to  $[101]$ ,  $[112]$  and  $[101]$ , respectively. Austenite grains and packets<sup>23,24)</sup> are seen in every specimen of Fig. 5. Martensite blocks<sup>23,24)</sup> are also seen clearly in the 0.36% crept specimen, and the block-like substructure is seen in both the 2.1 and 17.7% crept specimens. But in the 2.1% crept specimen fine substructures are seen within the block-like structures. In order to visualize the substructure, the orientation for each substructure has been investigated exactly.

Figure 6 shows the grain color maps with grain tolerance angle set to 5 degrees for the same areas of the specimens shown in Fig. 5. The grain tolerance angle defines a grain by specifying the minimum misorientation value that was caused by a grain boundary. Measurements with misorientations below this value are grouped together and grains are defined. The grain tolerance angle however can be set at values below what is considered a high-angle grain boundary to define visually sub-grain structure as well. The shape of

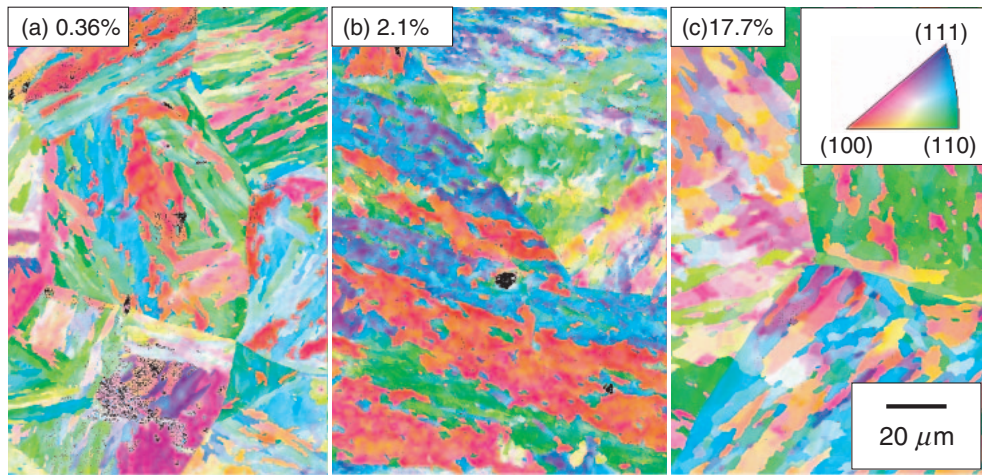


Fig. 5 Sample normal crystal direction maps for F82HD crept for (a) 0.36%, (b) 2.1% and (c) 17.7%.

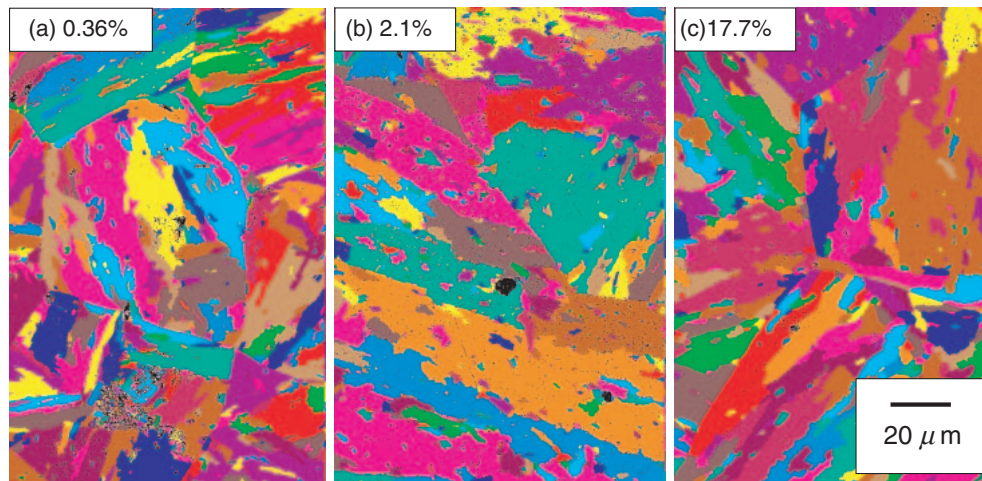


Fig. 6 Grain color maps with grain tolerance angle of 5 degrees for F82HD crept for (a) 0.36%, (b) 2.1% and (c) 17.7%.

lath block is rather sharp and their boundaries look like zigzag in transition creep, *i.e.* 0.36% (Fig. 6(a)). In the 2.1% crept specimen, the lath blocks seem to grow enveloping small islands within themselves. In acceleration creep the blocklike substructure seems to be polygonized and the shape of the lath blocks becomes roundish as compared with that of the transition creep and the size of block-like structure decreases again. Figure 7 shows the comparative correlated misorientation angle distributions with 5 degrees of the minimum misorientations at 850X magnification. It is found that when the creep strain is 2.1%, the number of large angle boundary shows minimum and the number of small angle boundary is the maximum. Therefore, it is necessary to investigate the grain color map with finer grain tolerance angle than 5 degrees as shown in Fig. 6.

Figure 8 shows the grain color maps with grain tolerance angle set to 0.5 degrees for the specimens shown in Fig. 6. Grain color maps for 0.36 and 17.7% look similar to those for 5 degrees except for that the grain sizes decrease. For the 2.1% crept specimen, excepting the region with grains of several micrometers, a lot of ultra fine grains the size of which are below 1  $\mu\text{m}$  are uniformly dispersed through the specimen. Similar ultra fine grains are also partially found in

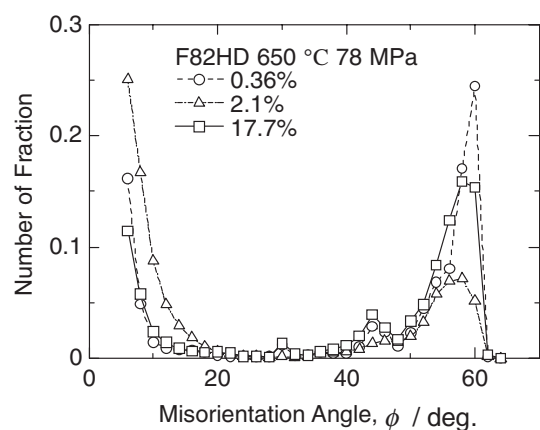


Fig. 7 Comparative correlated misorientation angle distributions with 5 degrees minimum misorientations for F82HD at 850X magnification.

the specimen crept for 0.36% (Fig. 8(a)).

The average grain diameter was calculated as 15.0, 25.7 and 20.4  $\mu\text{m}$  for the 0.36, 2.1 and 17.7% crept specimens, respectively, using the grain size histogram corresponding to Fig. 6 (grain tolerance angle is 5 degrees). However, the area



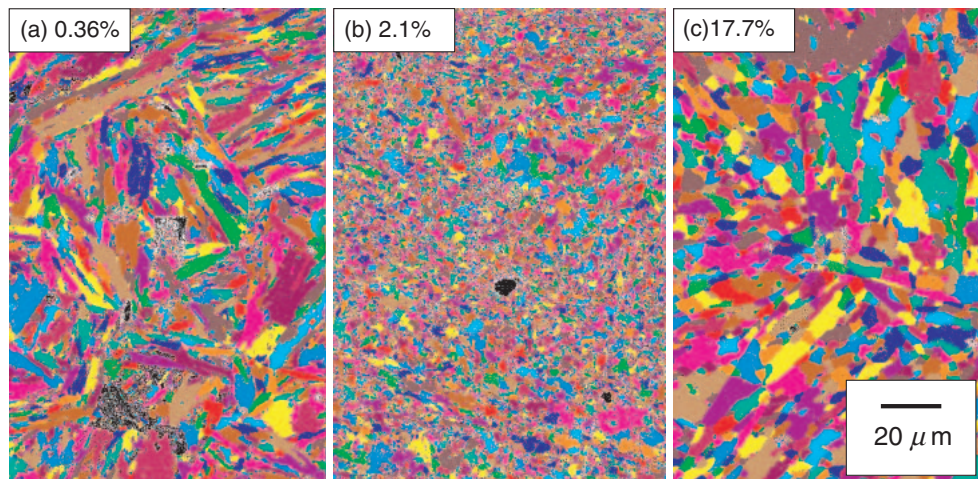


Fig. 8 Grain color maps with grain tolerance angle of 0.5 degrees for F82HD crept for (a) 0.36%, (b) 2.1% and (c) 17.7%.

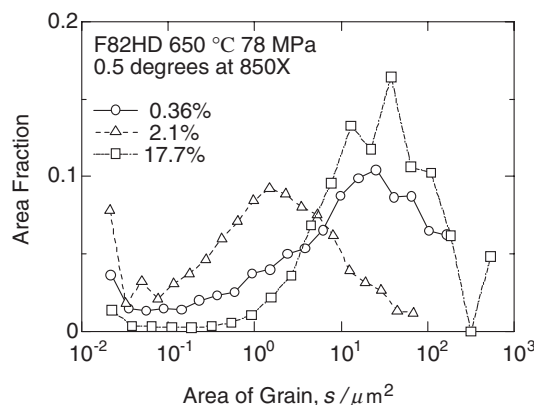


Fig. 9 Grain size histograms with grain tolerance angle of 0.5 degrees for F82HD crept for (a) 0.36%, (b) 2.1% and (c) 17.7%. The average grain diameter is (a) 5.0  $\mu\text{m}$ , (b) 1.8  $\mu\text{m}$  and (c) 7.4  $\mu\text{m}$  and average grain area is (a) 32.3  $\mu\text{m}^2$ , (b) 5.0  $\mu\text{m}^2$  and (c) 73.6  $\mu\text{m}^2$  in area fractions.

fraction increased with increase in grain area and did not show the maximum at the moderate position in a horizontal axis. Therefore, the average grain diameters, in this case, are meaningless. Figure 9 shows the grain size histogram corresponding to Fig. 8, where the observed area for each grain is plotted in the horizontal axis. The average grain diameter, which is measured using Fig. 9, is 5.0, 1.8 and 7.4  $\mu\text{m}$  for the 0.36, 2.1 and 17.7% crept specimens, respectively. These histograms show that beside the grains of which area is larger than 0.1  $\mu\text{m}^2$  the ultra fine grains of the area of the order of 0.02  $\mu\text{m}^2$  exist for every specimen and the area fraction of the ultra fine grain seems to be the maximum near the strain where the creep rate is minimum.

## 4. Discussion

### 4.1 Change in grain size during creep deformation

It is reported that lath width of high chromium martensite steel continuously increases from 0.5 to about 1  $\mu\text{m}$  with increasing creep strain,<sup>13–17)</sup> though the lath width of the previous works is rather small as compared with F82HD and, moreover, lath width in transition creep has been hardly reported.

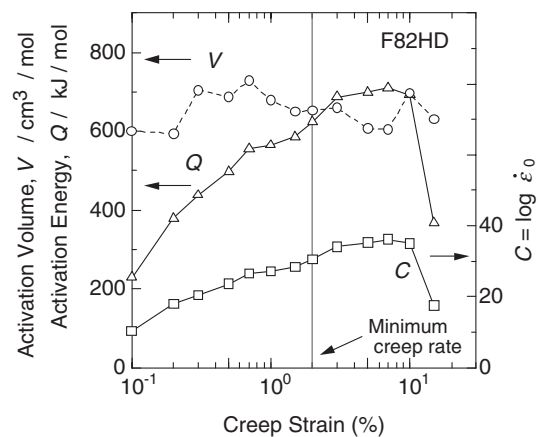


Fig. 10 Activation energy,  $Q$ , activation volume,  $V$ , mobile dislocation density parameter,  $C$ , as a function of creep strain for F82HD.

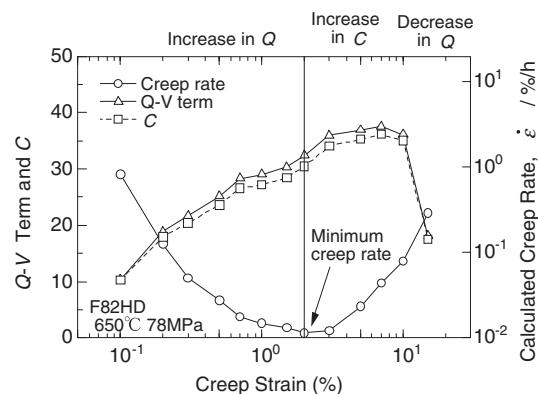


Fig. 11 The  $Q - V$  term,  $C$  and calculated creep rate as a function of creep strain.

On the other hand, the X-ray and EBSD measurements for F82HD clearly indicate that the particle or grain size shows minimum at minimum creep rate. As mentioned in the previous section, grain size by EBSD depends on grain tolerance angle, scanning distance per each step and scanning area and, as a consequence, the average grain size by EBSD for 5 degrees was statistically vague. However, it is found

from Figs. 4, 8 and 9 that grain size obtained by X-ray roughly agrees with grain size obtained by EBSP for 0.5 degrees.

Nakashima *et al.*<sup>25)</sup> reported the micro-structural change of the modified 9Cr-1Mo martensitic steel during creep at about 667°C using an SEM-EBSP system, however they did not observe ultra fine grains as shown in Fig. 8(b). The major reason for this is that their scanning step was 0.5 µm, 5 times larger than that of present study.

Integrated width of martensitic steel as normalized state is generally very large, which is caused by strains due to martensite. The integrated width decreases to a certain value with the advance of tempering. When particles are growing, the particles collide with each other, which may generate elastic strain. This process induces the creation of new fine grains during high temperature creep as shown in Fig. 8(b). After this process the fine grains grow further and particle size or grain size increases again as shown in Figs. 8 and 9. These processes are supported by both the X-ray data shown in Fig. 4 and the change in the preferred orientation during creep deformation measured by EBSP.

These facts suggest that the process of grain growth and subsequent creation of new fine grains is an essential process for the recovery of martensite, however the causal relationship between the creation of the fine grains and the occurrence of minimum creep rate is not always clear.

#### 4.2 Analysis of creep curves of F82HD

Time to rupture,  $t_r$ , has been formulated by the power law for a long time. However, recently availability of a following exponential equation for fitting  $t_r$  has been re-confirmed.<sup>26,27)</sup>

$$t_r = t_{r0} \exp\{(Q - \sigma V)/RT\}, \quad (1)$$

where  $t_{r0}$ ,  $Q$ ,  $\sigma$ ,  $V$ ,  $R$  and  $T$  are the pre-exponential factor, the apparent activation energy, applied stress, the activation volume, the Gas constant and absolute temperature, respectively, and

$$C = -\log t_{r0}. \quad (2)$$

The advantages of the exponential equation are as follows: firstly it is helpful for extrapolating long-term rupture strength, because stress is correlated linearly with the logarithm of time to rupture and secondly, the material constants,  $Q$ ,  $V$ ,  $C$ , which are calculated from the exponential equation, can help the interpretation of rupture behavior.

The exponential equation is also applicable to minimum creep rate and it is also easy to imagine that the creep rate at a given strain follows the exponential equation. That is,

$$\dot{\epsilon} = \dot{\epsilon}_0 \exp\{-(Q - \sigma V)/RT\}, \quad (3)$$

where  $\dot{\epsilon}_0$  is the pre-exponential factor and  $C$  is defined as  $C = \log \dot{\epsilon}_0$ . Material constants,  $Q$ ,  $V$ ,  $C$  were calculated using the creep curves for F82HD and the results are plotted in Fig. 10 as a function of creep strain.

Both  $Q$  and  $C$  increase with increasing creep strain and show the maximum near 7%, and finally both decrease.  $V$  shows the maximum near 0.6%, though the change is not so large. We found that, on the contrary to our expectations, the material constants,  $Q$ ,  $V$ ,  $C$ , vary largely with increasing creep strain. It is not a common sense that  $Q$  increases up to

about 7% beyond the strain at minimum creep rate, *i.e.* 2%, because increasing in  $Q$  is considered to relate with the increase in resistance to mobile dislocations. Therefore, further discussion is necessary.

#### 4.3 Rate-controlling factor in creep rate

From eq. (3) we obtain

$$\log \dot{\epsilon} = C - \left( \frac{Q}{2.3RT} - \frac{\sigma V}{2.3RT} \right), \quad (4)$$

or

$$T(-\log \dot{\epsilon} + C) = \frac{Q}{2.3R} - \frac{\sigma V}{2.3R}. \quad (5)$$

The left hand side of eq. (5) corresponds to the well known Larson-Miller parameter and, therefore, the value of  $C$  for rupture data is known as about 20 for usual steels and about 30 for high chromium steels.<sup>26)</sup> Therefore, it is not so strange that the observed value of  $C$  for F82HD is ranging from 10 to 35. Equation (3) is introduced from the well known relation,  $\dot{\epsilon} = \rho b v$ , assuming the thermal activation process for dislocation motion, where  $\rho$ ,  $b$  and  $v$  are mobile dislocation density, the Burgers vector and dislocation velocity given by  $v = v_0 \exp\{-(Q - \sigma V)/RT\}$ . Therefore, we obtain

$$C = \log(\rho b v_0). \quad (6)$$

Equation (6) denotes that the Larson-Miller constant  $C$  is a parameter representing the mobile dislocations density, MDDP, assuming that  $b$  and  $v_0$  are constant. In Fig. 11 the 1<sup>st</sup> and 2<sup>nd</sup> terms of eq. (4) are plotted as a function of creep strain and calculated creep rate using the calculated  $Q$ ,  $V$ ,  $C$  is also plotted. In the figure the subtraction of  $Q - V$  term from  $C$  is corresponding to the logarithm of the creep rate. Below 2% of creep strain, *i.e.* transition creep range increase in  $Q - V$  term controls the creep rate, because the increase in  $C$ , *i.e.* MDDP, observed in transition creep cannot explain decrease in creep rate. In the strain range of 2 to 7%, increase in both  $Q - V$  term and  $C$  is observed, however the increase in  $C$  is larger than that of  $Q - V$  term and, therefore, creep rate is accelerating, *i.e.* only the increase in MDDP can explain the acceleration creep. In the strain range over 7% it is clear that the decrease in  $Q - V$  term controls the creep rate.

#### 4.4 Microstructural changes for F82HD during creep

In the previous section it is concluded that the increase in  $Q - V$  term is rate-controlling factor for the transition creep rate. The increase in  $Q - V$  term implies that the increase in the resistance to the dislocation motion of F82HD. However, hardness, X-ray and EBSP observations show that hardness decreases and the particle size increases followed by a decrease within the transition creep range, however we have not yet a clear explanation for the continuous decrease in creep rate in transition creep range.

Tamura *et al.*<sup>28)</sup> showed that the actual obstacle spacing to the dislocation motion,  $d$ , can be calculated using the values of  $Q$  and  $V$  obtained from rupture data. If this idea can be expanded to the creep rate observed, then we obtain

$$\frac{d}{p} = \frac{\mu b}{\pi(1 - \nu)} \ln\left(\frac{d}{r_0}\right) \frac{V}{Q_{\text{int}}}, \quad (7)$$

and

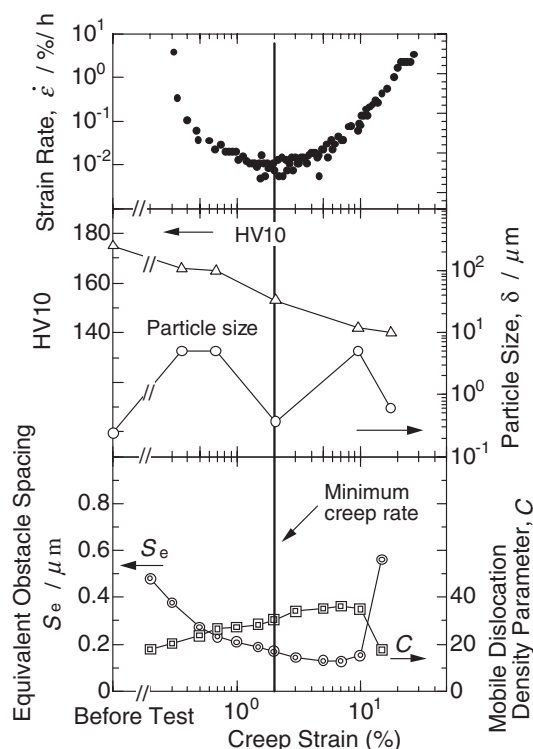


Fig. 12 EOS and MDDP as a function of creep strain comparing with the metallurgical properties.

$$Q = Q_d + Q_{\text{int}} \left( 1 - \frac{d \ln \mu}{d \ln T} \right), \quad (8)$$

where  $\mu$ ,  $\nu$ ,  $r_0$ ,  $Q_d$  are the shear modulus, the Poisson's ratio, the length between nearest neighbor atoms and the activation energy of self-diffusion, respectively. The parameter,  $p$ , is an adjustable parameter depending on the characters of obstacles and dislocations. Tamura *et al.*<sup>22)</sup> named  $d/p$  of eq. (7) as Equivalent Obstacle Spacing (EOS,  $S_e$ ), because it is difficult to calculate the value of  $p$  exactly, but the values of EOS can be estimated using only experimental data. The values of EOS for several alloys roughly coincide with the observed inter-particle spacing or sub-grain size, *i.e.*  $p \approx 1$ .<sup>22)</sup>

$$S_e \equiv d/p \quad (9)$$

Figure 12 shows the summary for F82HD. In the figure together with the hardness change typical properties are shown as a function of creep strain. Hardness decreases clearly and the particle size measured by XRD shows bimodal change. In the figure EOS and MDDP are also plotted.

EOS decreases in transition creep and, on the contrary, MDDP increases. The decrease in hardness and the increase in MDDP cannot explain the decrease in creep rate in transition creep. The decrease in both particle size and EOS should be responsible for the decrease in creep rate in transition creep. Initial tempered martensite structure is rearranged during creep deformation, new fine grains with less elastic strains are gradually formed and the new fine grains cover whole of the specimen when the specimen is crept near the strain where the creep rate is minimum as

shown in Figs. 4, 8, 9. The average diameter of the new fine grains is about 1 or 2  $\mu\text{m}$  as shown in Figs. 8, 9.

However, the calculated values of EOS are decreasing from 0.5 to 0.15  $\mu\text{m}$  during transition creep. The attained value of EOS near the minimum creep rate strain is comparable to the inter-precipitated-particle distance of the creep-ruptured specimen of F82HD, *i.e.* about 0.4  $\mu\text{m}$ .<sup>22)</sup> This implies that dislocations may not feel the new fine grain boundaries as strong obstacles, of which average grain diameter is about 1–2  $\mu\text{m}$ . However, the change in EOS indicates that mobile dislocations should recognize the gradual creation of some new strong obstacles by a process like “work hardening” during transition creep. The mobile dislocations tangle with the particles that are precipitated with intervals of 0.4  $\mu\text{m}$ <sup>22)</sup> and form new obstacle nets of sessile dislocations, which should become the new strong obstacles. This may be a possible mechanism for the work hardening.

In Fig. 9 beside the main peak of newly formed fine grains we can find in the 2.1% crept specimens the considerable amount of the ultra fine grains of which average area is 0.02  $\mu\text{m}^2$  or average size is 0.14  $\mu\text{m}$ . This may correspond to the visual evidence for the very small values of EOS.

In acceleration creep though both hardness and particle size decrease with increase in creep strain, EOS still decreases slightly up to 7%. This cannot explain the acceleration of creep rate. The value of  $C$ , MDDP, is increasing with increase in creep strain and, therefore, increase in mobile dislocation density may be the main cause for the acceleration of creep rate in F82HD. When creep strain is larger than 7%, EOS increases again and MDDP decreases. In this case, the increase in EOS may contribute the acceleration of creep rate. However, in this range necking may occur, we cannot conclude a rate-controlling factor exactly. The change of MDDP in acceleration creep is moderate as compared with that of transition creep, and so, it is natural to feel a question concerning how the small increase in MDDP can fully explain the increase in creep rate in acceleration creep range. However, as shown in Fig. 11, creep rate is always determined by the difference of two opposite factors, *i.e.* accelerating factor and slowing down factor. Therefore, the question should be solved easily.

#### 4.5 Change in $Q$ , $V$ and $C$ for simply tempered F82HS during creep

Figure 13 shows the change in  $Q$ ,  $V$  and  $C$  for F82HS as a function of creep strain. All these material constants roughly decrease with increasing creep strain, which is much different from the behavior of F82HD. Generally it is accepted that transition creep of martensitic steel is explained by the decrease in excess dislocation density, which is introduced by normalizing.<sup>13)</sup> In this sense the creep behavior of F82HS is standard one.

#### 4.6 Relation between EOS and MDDP

It has been clarified from the above discussion that creep curves of F-82H can be explained by the changes in both EOS and MDDP which represent the creep resistance against the mobile dislocations and mobile dislocation density itself, respectively. The values of EOS are roughly supported by the

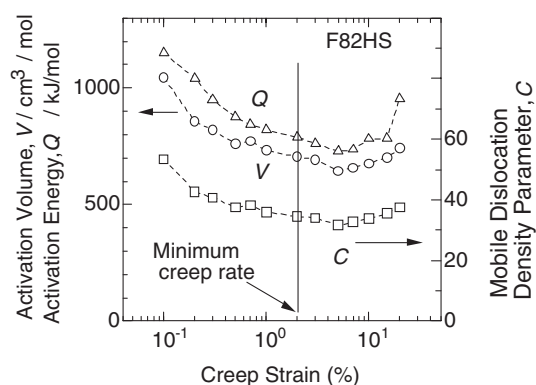


Fig. 13 Activation energy,  $Q$ , activation volume,  $V$ , and mobile dislocation density parameter,  $C$ , as a function of creep strain for F82HS.

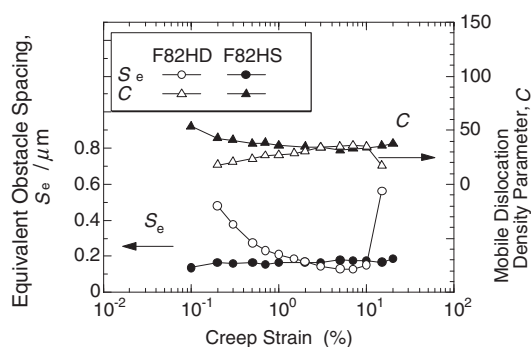


Fig. 14 Comparison of EOS and MDDP as a function of creep strain for two martensitic steels with different heat treatments, F82HD and F82HS.

TEM observations.<sup>22)</sup> However, MDDP has not been verified metallurgically. In order to clarify this point the values of EOS and MDDP for F82HS are re-plotted in Fig. 14 comparing with those for F82HD. EOS for F82HD decreases and MDDP increases during transition creep. Therefore, the decrease in EOS during transition creep is responsible for the decrease in creep rate of F82HD. On the contrary, the values of EOS and MDDP for F82HS change oppositely with each other. In this case the increase in EOS cannot explain the decrease in creep rate during transition creep, therefore the decrease in MDDP is responsible for the decrease in the creep rate in transition creep. F82HS was not pre-tempered at 550°C before tempering at 800°C and, therefore, may not precipitate fine  $M_{23}C_6$  particles. Thus, in F82HS the decrease in EOS, which implies that the “work hardening”, does not occur and on the contrary the decrease in MDDP, which denotes the decrease in a lot of induced dislocations formed during normalization, does occur during transition creep. That is, dynamic recovery may occur during transition creep of F82HS, which is the origin of the decrease in creep rate during transition creep. Abe *et al.*<sup>13)</sup> observed the creep behavior of a martensitic 9Cr-2W steel and concluded that the transition creep was a consequence of the movement and annihilation of excess dislocations. The observed results and interpretation on the 9Cr-2W steel can be used to the explanation of the transition creep behavior of F82HS.

However, the annihilation process is not the only explanation to the transition creep for martensitic steel in general. The decrease in EOS, which means the increase in resistance

against mobile dislocations with increase in creep strain during transition creep, *i.e.* work hardening, should possibly occur in martensitic steel, as shown in Figs. 8–12. Similar phenomena shown in Fig. 14 have been observed in two kinds of modified 9Cr steels with different heat treatment.<sup>29)</sup>

As shown in Fig. 14 EOS and MDDP behave oppositely with each other with increase in creep strain. That is, when EOS increases, MDDP decreases and *vice versa*. Creep rate is a product of dislocation density and the velocity. The mobile dislocation density is a function of MDDP and the dislocation velocity is a function of EOS. Therefore, there should be a specific relation between these two parameters.

If we compare creep rate to an amount of the carriage of goods through a given road per unit time, when the number of cars increases (increases in mobile dislocation density, MDDP), the road gets choked and therefore the speed of cars slow down (decrease in equivalent obstacle spacing, EOS, and therefore decrease in dislocation velocity) and on the contrary when the number of cars decreases (decreases in MDDP), the road becomes deserted (increase in EOS). The width of a road also affects the total traffic per unit time (creep rate) and the width of the road can be compared to temperature and stress. The total traffic per unit time (creep rate) should depend on the number of cars and the speed of cars. The number of a signal mechanism or the conditions of the road also affects the traffic. However, essentially one of the two parameters, *i.e.* the number of cars or the speed of cars; which correspond to MDDP and EOS, respectively, is always a rate-controlling factor for the total traffic, that is, creep rate of material, even if it is in transition creep or in acceleration creep.

## 5. Conclusions

Creep curves of a double tempered 8%Cr-2%W-0.2%V-0.04%Ta martensitic steel have been analyzed and the metallurgical observations have been made for the specimens crept at approximately 650°C. These data were compared with the normally tempered steel and following conclusions are obtained.

- (1) Creep rupture strength of the double tempered steel is slightly higher than that of the normally tempered one due to the finely dispersion of  $M_{23}C_6$  and the creep curves of the double and normal tempered steels are much different with each other.
- (2) Hardness of the double tempered steel decreases with increasing creep strain and the changes in TEM observation are similar to the literatures.
- (3) Super fine sub-grains of the order of 1  $\mu\text{m}$  are formed near the creep strain at minimum creep rate, which was newly found by EBSP and X-ray measurements.
- (4) Two parameters, equivalent obstacle spacing, EOS, and mobile dislocation density parameter, MDDP, have been calculated from the activation energy, the activation volume and the pre-exponential term of an exponential type creep equation. These two parameters change oppositely during the advance of creep deformation with each other. During transition creep, decrease in EOS or MDDP with increasing strain causes the decrease in creep rate, which depends on the



initial condition of materials. On the other hand, during acceleration creep, increase in EOS or MDDP is a rate-controlling factor to determine creep rate.

- (5) Decrease in creep rate in transition creep of the double tempered steel cannot explain directly the observed decrease in dislocation density and hardness. Transition creep of the double tempered steel can be explained by decrease in EOS with increase in creep strain.
- (6) Both EOS and MDDP are representative parameters of the change in substructure during creep deformation of martensitic steel.

## REFERENCES

- 1) M. Tamura, H. Hayakawa, M. Tanimura, A. Hishinuma and T. Kondo: J. Nucl. Mater. **141–143** (1986) 1067–1073.
- 2) M. Tamura, H. Hayakawa, A. Yoshitake, A. Hishinuma and T. Kondo: J. Nucl. Mater. **155–157** (1988) 620–625.
- 3) H. Hayakawa, A. Yoshitake, M. Tamura, S. Natsume, A. Gotoh and A. Hishinuma: J. Nucl. Mater. **179–181** (1991) 693–696.
- 4) K. Shiba, M. Enoeda and S. Jitsukawa: J. Nucl. Mater. **329–333** (2004) 243–247.
- 5) T. Hatano, S. Suzuki, K. Yokoyama, T. Kuroda and M. Enoeda: J. Nucl. Mater. **283–287** (2000) 685–688.
- 6) Y. Nomoto, S. Suzuki, K. Ezato, T. Hirose, D. Tsuru, H. Tanigawa, T. Hatano, M. Enoeda and M. Akiba: Fusion Engineering and Design **81** (2006) 719–724.
- 7) V. K. Sikka, C. T. Ward and K. C. Thomas: *Ferritic Steels for High-Temperature Application*, (American Society for Metals, Ohio, 1983) pp. 65–83.
- 8) K. P. Balan, A. Venugopal Reddy and D. S. Sarma: J. Mater. Eng. & Perform **8** (1999) 385–393.
- 9) Y. Kadoya, B. F. Dyson and M. McLean: Met. Mater. Trans. A **33A** (2002) 2549–2557.
- 10) S. Jitsukawa, M. Tamura, B. van der Schaaf, R. L. Klueh, A. Alamo, C. Petersen, M. Schirra, P. Spaetig, G. R. Odette, A. A. Tavassoli, K. Shiba, A. Kohyama and A. Kimura: J. Nucl. Mater. **307–311** (2002) 179–186.
- 11) S. Jitsukawa, A. Kimura, A. Kohyama, R. L. Klueh, A. A. Tavassoli, B. van der Schaaf, G. R. Odette, J. W. Rensman, M. Victoria and C. Petersen: J. Nucl. Mater. **329–333** (2004) 39–46.
- 12) R. L. Klueh and D. R. Harries: *High-chromium Ferritic and Martensitic Steels for Nuclear Applications*, (ASTM, West Conshohocken, 2001) pp. 1–217.
- 13) F. Abe, S. Nakazawa, H. Araki and T. Noda: Met. Trans. A **23A** (1992) 469–477.
- 14) K. Sawada, K. Maruyama, R. Komine and Y. Nagae: Tetsu-to-Hagane **83** (1997) 466–471.
- 15) K. Sawada, M. Takeda, K. Maruyama, R. Komine and Y. Nagae: Tetsu-to-Hagane **84** (1998) 580–585.
- 16) Y. Kadoya and E. Shimizu: Tetsu-to-Hagane **86** (2000) 189–195.
- 17) T. Endo, F. Masuyama and K. Park: Tetsu-to-Hagane **88** (2002) 526–533.
- 18) N. Yamanouchi, M. Tamura, H. Hayakawa, A. Hishinuma and T. Kondo: J. Nucl. Mater. **191–194** (1992) 822–826.
- 19) W. H. Hall: The Proceedings of the Physical Society **62** (1949) 741–743.
- 20) M. Tamura, K. Shinozuka, H. Esaka, S. Sugimoto, K. Ishizawa and K. Masamura: J. Nucl. Mater. **283–287** (2000) 667–671.
- 21) B. Sundman, B. Jansson and J.-O. Andersson: CALPHAD **9** (1985) 153–190.
- 22) M. Tamura, H. Sakasegawa, Y. Kato, A. Kohyama, H. Esaka and K. Shinozuka: ISIJ Int. **42** (2002) 1444–1451.
- 23) J. M. Marder and A. R. Marder: Trans. ASM **62** (1969) 1–10.
- 24) T. Maki, K. Tsuzaki and I. Tamura: Trans. ISIJ **20** (1980) 207–214.
- 25) H. Nakashima, D. Terada, F. Yoshida, H. Hayakawa and H. Abe: ISIJ Int. **41** (2001) S97–S100.
- 26) M. Tamura, H. Esaka and K. Shinozuka: ISIJ Int. **39** (1999) 380–387.
- 27) M. Tamura, H. Esaka and K. Shinozuka: Mater. Trans. **44** (2003) 118–126.
- 28) M. Tamura, H. Esaka and K. Shinozuka: Mater. Trans. JIM **41** (2000) 272–278.
- 29) M. Tamura, H. Sakasegawa, A. Kohyama, K. Shinozuka and H. Esaka: TMS Letters, (2004). 5<sup>th</sup> issue.